Exploring the Anomalous Phase Behavior of High-Pressure Ices in Diamond Confinement

Amrita Goswami and Jayant K. Singh*

ACCESS | Metrics & More | Article Recommendations | Supporting Information

ABSTRACT: Inspired by the discovery of high-pressure ice inclusions in diamond, we investigate the rich structural diversity of high-pressure phases of quasi-two-dimensional water constrained by diamond matrices, using molecular dynamics simulations. Monolayer ices formed are structurally similar to monolayer ices constrained by graphene. We report new bilayer and trilayer ice phases, specifically, the AB II, ABC I, ABC II, and AAB/ABB ordered phases. The relative stability of the interlayer hydrogen bonds between adjacent layers reveals differences in structural properties. We observe grain-boundary migration between pockets of AAB and ABB ices, during the pressurization process. The compression-limit phase diagram in the slit width−lateral pressure plane has been constructed and analyzed. Our results indicate that the phase behavior of confined ice is qualitatively independent of the diamond−water force-field parameters and is significantly influenced by the lattice structure and geometry of the confining surfaces.
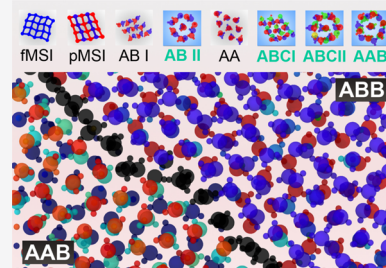
INTRODUCTION

Naturally occurring high-pressure phases of ice are extremely rare.[1] The thickest ice sheets on Earth are 3.5 km thick, which is much less than the 22 km thickness required to create a sufficiently high pressure for the formation of the high-pressure ice II or III.[2] It has been hypothesized that ice VII, the densest known ice polymorph,[3] exists within cold subconducting slabs as a consequence of minerals undergoing dehydration reactions.[4]

The first naturally occurring ice VII has been discovered recently as diamond inclusions.[5] In a previous study, the spectral signature of another high-pressure ice polymorph, ice VI, was observed when inclusions in cuboid diamond were analyzed.[6] Aqueous fluid is trapped in diamonds at the lower mantle or transition zone, where the pressure and temperature are extremely high.[7,8] During the ascent of the diamonds to upper regions of the lithosphere, the temperature decreases, causing the fluid inclusions to crystallize. Rigid diamond host crystals constrain the pressure of the encapsulated fluids, providing the high pressure required for the freezing of rare high-pressure ice polymorphs.

Water and its solid crystalline polymorphs show considerable diversity, and to date, there have been 17 experimentally confirmed ices.[9] Restrictions on the local environment impart even more complexity to the behavior of confined water,[10] which is markedly different from the phase behavior of bulk water. A rich multitude of distinct phases under confinement has been experimentally predicted[11,12] and observed in simulations.[13−15] Several phases obtained in confinement are not observed when bulk water is frozen in ambient conditions. Quasi-two-dimensional water, constrained within a slit width of 6−7 Å, exhibits a plethora of exotic ordered phases in simulations, reportedly forming hexagonal monolayer, pentag-onal Cairo-tiled, flat-square, and rhombic structures.[13,15−19] Bilayer and trilayer ices formed in confinement also form several interesting ordered structures,[20−24] including a square trilayer ice with ABA stacking, resembling a clathrate-like structure.[25] The templating effects of the surface, as well as the confinement width, have been reported to influence the structure of ice.[16]

The regime of interest indicated by experimental discoveries, for high-pressure water confined by diamond, has not previously been explored. In this work, we investigate, for the first time, the structures of ice formed in confinement by model diamond surfaces, under gigapascal (high) pressure, using molecular dynamics simulations. We report new bilayer and trilayer ices, which have not been previously observed in simulations.

COMPUTATIONAL DETAILS

Construction of Model Diamond Surfaces. The model diamond surfaces were created using experimental cell parameters and lattice positions.[26] The diamond lattice structure was obtained from the Crystallography Open Database.[27] The dimensions of the model diamond sheets were 74.902 Å × 74.902 Å in the X and Y dimensions, respectively.

Simulation Setup. Our simulation setup is similar to analogous systems prepared for trilayer graphene sheets.[28] The XZ-plane and XY-plane views of a representative simulation system are shown in Figure 1a,1b, respectively. A nanochannel
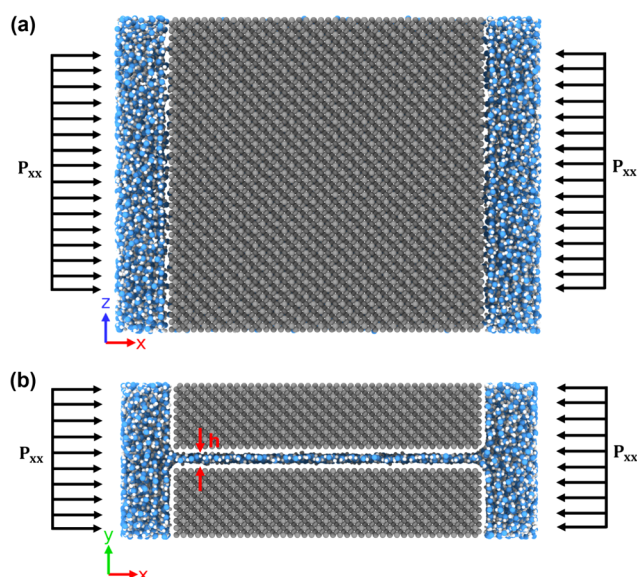
Figure 1. Representative views of the simulation system configuration used. The carbon atoms of the diamond surface are colored in gray; the oxygen atoms are blue; and the hydrogen atoms are white. (a) Top view of the simulation system, showing the XZ plane. (b) Side view of the simulation system, showing the XY plane. The center-to-center slit width between the parallel diamond layers is h.

was created by introducing a slit width, h, between a pair of four-layered sheets of the model diamond lattice. Two water reservoirs, containing 2000−4000 molecules, were placed on either side of the nanochannel thus formed. The center-to-center slit width between the parallel diamond sheets was varied from 6 to 11.5 Å. These slit widths are sufficiently large to allow monolayer, bilayer, trilayer, and tetralayer ice structures to form within the nanochannel. In this work, we focus on monolayer, bilayer, and trilayer ices.

We have used LAMMPS[29] to run equilibrium molecular dynamics simulations. Lateral pressures were applied in the X dimension. The molecular dynamics (MD) simulations were performed in the isothermal−isobaric ($NP_{xx}T$) ensemble. The temperature (T) and pressure (P_{xx}) were controlled by the Nose−Hoover thermostat and barostat, respectively. A time step of 1 fs was used for the velocity Verlet integration scheme. The particle−particle−particle mesh (PPPM) algorithm was used for computing the long-range interactions.

TIP4P/2005 was used to model the water molecules in our system.[30] Among the commonly used rigid water models for simulating confined systems, TIP4P/2005 performs reliably well,[31] correctly reproducing the experimentally observed AA bilayer stacked ice structure in graphene nanoconfinement.[11] The sum of the interactions between the TIP4P/2005 molecules and the external Lennard-Jones (LJ) potential of interaction between the water molecules and the diamond sheet yield the total potential of interaction.

Excavated natural diamonds can be either hydrophobic or hydrophilic in nature, with a tendency to be hydrophilic for alluvial diamonds, and hydrophobic for kimberlite pipe diamonds.[32]

In this work, we have used the parameters reported by Werder et al.[33] to model the LJ interaction between the oxygen atoms of water and the carbon atoms of the diamond. These parameters have been extensively used for graphite and water, accurately reproducing the contact angle of water on graphite.[20,25,28,34]

Since the wettability behavior of natural diamonds is highly variable,[35−37] we have also used different ϵ_{CO} values, as shown in Table 1. The Case II parameters model a highly hydrophobic

Table 1. Parameters

name	ϵ_{CO} (kcal/mol)
Case I	0.09369
Case II	0.02890
Case III	0.58790

surface, while the Case III parameters are for a hydrophobic sheet. Unless otherwise mentioned, the graphite−water parameters proposed by Werder et al.[33] have been used, and henceforth referred to as Case I.

We have used OVITO[38] for generating the visuals in this work. Primitive rings were obtained and further analyzed according to our topological network criterion for quasi-two-dimensional systems,[39] using a FOSS molecular dynamics analysis engine, d-SEAMS.[40]

RESULTS AND DISCUSSION

First, we investigate pressure-induced phase changes at a constant temperature of 300 K, by pressurizing and depressurizing systems with cross-interaction parameters representing varying hydrophobicity (Table 1). The pressure was changed in steps of 0.1 GPa, over 1 ns.

Figure 2 shows the trend in the change in potential energy per molecule with lateral pressure during the pressurization and
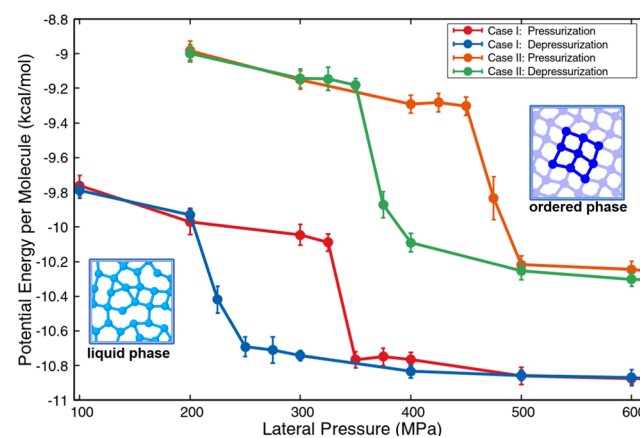

Figure 2. Change of potential energy per molecule with lateral pressure during pressurization up to 600 MPa. The pressurization and depressurization processes are shown in red and blue for Case I and in orange and green for Case II, respectively. The insets show representative views of the liquid phase and solid phase. For Case II, lateral pressures less than 200 MPa are not high enough for water to completely fill the capillary.

depressurization process in the range of 100−600 MPa for the hydrophobic Case I and highly hydrophobic Case II parameters. During the pressurization process, there is an abrupt decrease in energy, due to the formation of an ordered phase. The depressurization process is characterized by a concomitant sudden energy increase for both Cases I and II due to the breakdown of the ordered phase. A hysteresis loop is clearly evident from Figure 2, which is indicative of a first-order phase transition. Movie S1 documents the sudden formation of the ordered phase. The channel is fully or partially empty for
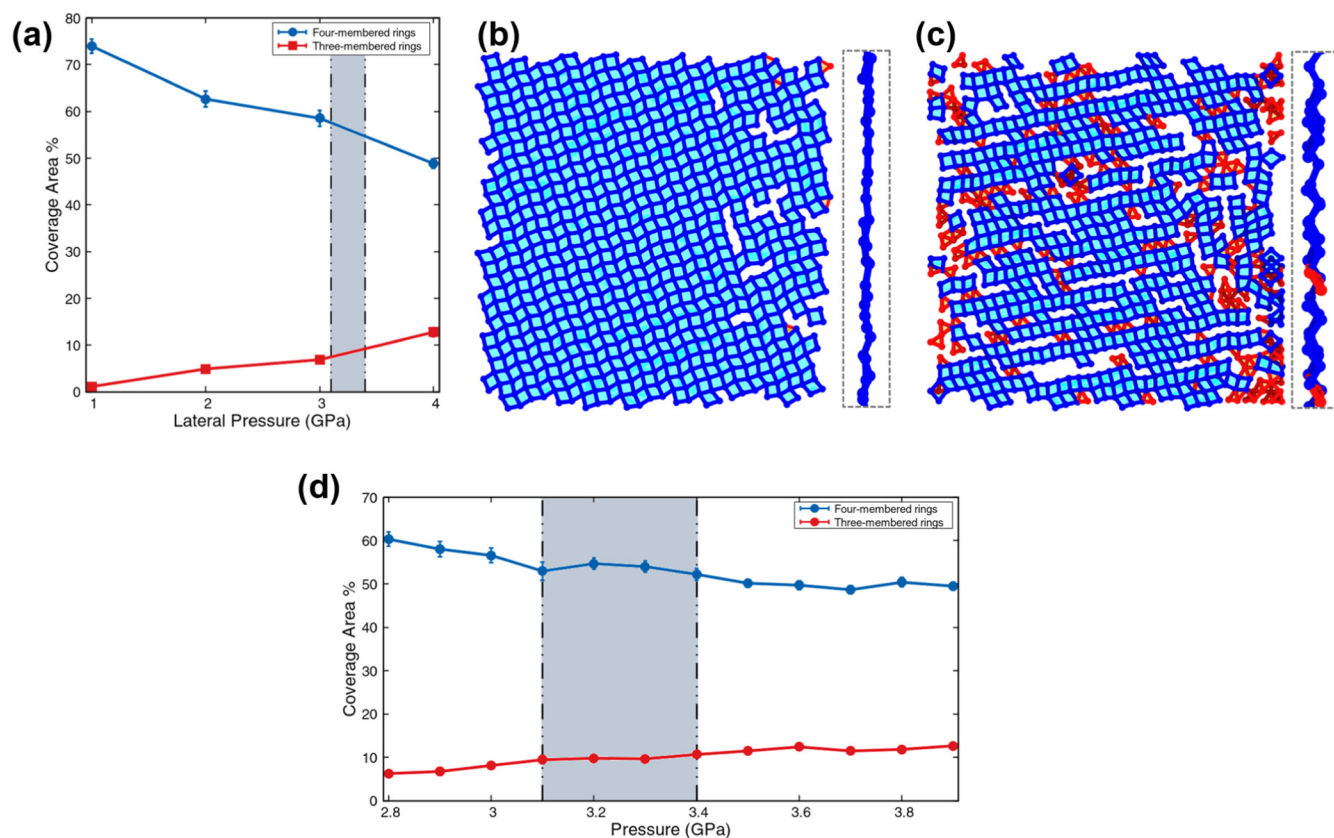
Figure 3. (a) Coverage area percentage of a monolayer for $h = 6$ Å, as a function of lateral pressure, at a constant temperature of 300 K. The pressure range 3.1−3.4 GPa, in which fMSI changes to pMSI, is highlighted. (b, c) Overhead XY plane views of the monolayer ice at lateral pressures of 1 and 4 GPa, corresponding to fMSI and pMSI. The insets show sections of lateral view of the monolayers in each case, depicting the flat and puckered nature in (b, c), respectively. The four-membered rings are shaded in cyan, and the three-membered rings are shaded in orange. (d) Coverage area percentage for $n = 4$ and $n = 3$, in the pressure range of 2.8−3.9 GPa. The window of pressure range during which the fMSI to pMSI solid-to-solid transition takes place is shaded in gray.

pressures less than 200 MPa for the Case II system. The hydrophilicity of Case III parameters is such that the ordered phase is formed instantaneously at 300 K and 1 atm.

For Cases I, II, and III, the final ordered structures formed after pressurization are identical. We have found that the average H−O−H angle (described pictorially in Figure S1) is $103 \pm 1°$ in the ice structures formed using Cases I, II, and III parameters. The observation that the structures are insensitive to values of the diamond−water interactions is not surprising, as the force field is considered to have a little effect on the qualitative nature of the phase diagram.[14,15] The compression limit of liquid water is observed to be higher for Case II than for Case I, due to the increased hydrophobicity of the confining diamond sheets for Case II.

Monolayer Ice. Figure S2 depicts the different types and structures of monolayer ice, flat monolayer square ice (fMSI) and puckered monolayer square ice (pMSI), observed for the diamond−water system. The fMSI and pMSI structures are similar to monolayer ices observed in graphene confinement.

For slit width $h = 6$ Å, we observe a solid-to-solid phase transition from fMSI to pMSI, as shown in Figure S3. This fMSI-to-pMSI transition has not been observed for lateral pressures less than 4 GPa in analogous graphene−water systems.

Ice phases in quasi-two-dimensional phases can be determined using primitive rings obtained from the hydrogen-bond network (HBN). Figure S4 shows why the number of n-

membered rings is a nondescriptive metric for quasi-two-dimensional ice classification.

To investigate the relative proportions of the dominant square and triangular ices, during this solid-to-solid phase transition, we employ the coverage area percentage,[39] an area-based metric of quasi-two-dimensional ice classification. The theoretical coverage percentage for any n-membered ring phase is 100%, corresponding to a state wherein the n-membered rings entirely cover the confining sheet area.

Although the topological network criterion does not explicitly differentiate between fMSI and pMSI, both being composed of four-membered rings, the coverage area metric is able to describe the fMSI-to-pMSI phase transition, predicted by the behavior of the potential energy per molecule (Figure S3). Figure 3a depicts the changes in coverage area percentage during the fMSI-to-pMSI phase transition, in the range of lateral pressure of 1−4 GPa. Views of the fMSI and pMSI structures observed at 1 and 4 GPa, respectively, are shown in Figure 3b,3c.

At 4 GPa, the monolayer is highly puckered. From the overall trend in the coverage area percentage in Figure 3a, it is evident that the sum of the areas of three-membered and four-membered rings is less than the total area of the diamond sheet. This is partly because of the existence of point defects, which fracture the HBN. In addition, tilted or puckered rings necessarily cause a slight loss of area. As the monolayer becomes progressively more puckered, with the increase in lateral pressure, the total summation of the coverage area of three-

membered and four-membered rings decreases. We attribute this decrease in net area to the increase in point defects and the puckered nature of the monolayer.

Figure 3a,3d shows that increasing the lateral pressure increases the relative percentage of the triangular ice phase. We also note that the triangular phase forms ridges between gaps in the network of four-membered rings, in the case of pMSI (Figure 3c).

Bilayer Ice. Three types of bilayer ice are observed for different slit widths, for $h \in [7, 8.8]$ Å subjected to $0.6 \leq P_{xx} \leq 2.8$ GPa. AB-bilayer ice and AA-bilayer ice have both been reported for ice confined within graphene. Figure 4a,4c depicts views of
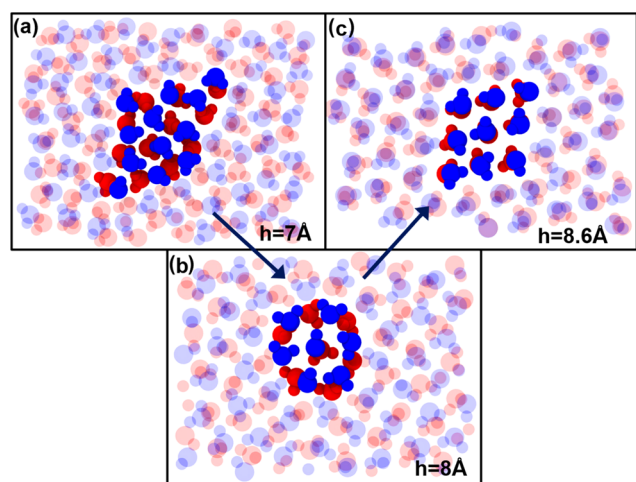

Figure 4. Comparison of bilayer ices formed. The arrows indicate the formation of each bilayer phase with increasing slit width, h. The oxygen and hydrogen atoms in the upper and lower layers are colored in blue and red, respectively. (a) Top view of AB-bilayer ice, formed at 3 GPa and 300 K, with $h = 7$ Å. AB-stacked bilayer ice is also observed within a graphene nanocapillary of width 8 Å, at 1.7 GPa and 300 K. (b) View of the XY plane, of a section of the bilayer ice formed between diamond layers with $h = 8$ Å, at 4 GPa and 300 K. The characteristic staggered hexagon structure is highlighted. This ice structure is unique to the diamond–water system. (c) Overhead view of AA-bilayer ice for $h = 8.6$ Å at 2 GPa. AA-bilayer ice is also formed within a graphene nanochannel with $h = 9$ Å.

AB-stacked and AA-stacked bilayer ices formed in diamond nanoconfinement. However, for $h = 7.6$–8.0 Å, a distinct type of bilayer ice is formed, exhibiting a peculiar "flowerlike" structure, as shown in Figure 4b. The bilayer ice shows neither strictly AA stacking nor AB stacking. This flowerlike structure is formed by a central molecule surrounded by six other molecules in the upper layer, below which the hexagon in the lower layer is staggered with respect to the upper hexagon. The central atoms in the upper and lower layers are connected by a hydrogen bond and show AA stacking. The surrounding hexagons are staggered with respect to each other and exhibit AB stacking. Henceforth, we refer to the true AB-stacked bilayer ice in Figure 4a as AB I and to the staggered hexagon structure in Figure 4b as AB II.

Figure 5 shows the HBN of individual layers of AB II and their relative orientations with respect to each other. Figure 5a,5c depicts the HBN of the upper and lower layers, respectively, of the AB II ice. In particular, the overlay of the fictitious line arrangement in Figure 5b,5d depicts how the peculiar staggered hexagon structure of AB II ice is formed because of the relative alignment of the upper and lower layers. Figure 5e,5f shows views of the entire bilayer ice structure, with the staggered

hexagon substructure highlighted. Figure S5 reaffirms that each layer of the bilayer ice has long-range order and an identical triangular arrangement.

Figure 6 shows the radial distribution functions ($g_{OO}(r)$) for AB I, AB II, and AA ices.

The first peak of $g_{OO}(r)$ for the AA-stacked ice is at 2.825 Å, with subsequent lower peaks at multiples of ≈ 2.825 Å. AA ice is very similar to the structure of the AA-stacked ice confined within a graphene nanocapillary.

The $g_{OO}(r)$ of AB II bilayer ice exhibits mingled characteristics of both AB I and AA bilayer ices, exemplified by Figure 6. The second maxima of $g_{OO}(r)$ is a split peak, whose twin peaks nearly coincide with corresponding shoulder peaks of $g_{OO}(r)$ of AB I and AA bilayer ices.

In Figure 7, the two peaks at ≈ 164 and $\approx 115°$ correspond to strong and weak hydrogen bonds.[13] The strong interlayer hydrogen bonds formed between water molecules directly over each other are in the perpendicular direction to the plane of the diamond surface. AB I bilayer ice has the highest relative proportion of weak inerratic hydrogen bonds, typified by the comparable heights of the two peaks in the interlayer angle distribution. The interlayer O–H⋯O angle distribution of AA ice has a single peak at 167.4°, and that of AB II ice has a shoulder peak. These trends show that AB II ice has strong inerratic hydrogen bonds, compared to AB I, while showing less strong interstratification than AA ice. The relative strength of interlayer hydrogen bonding reveals the intermediate nature of the AB II structure.

Trilayer Ice. For slit widths corresponding to $h \in [9, 11.1]$ Å, trilayer ices of three distinct forms are observed. On the basis of stacking order, we classify the trilayer ices as ABC I, ABC II, and AAB or ABB trilayer ices. These amorphous trilayer ices are different from the TL-ABA and TL-AAAI ices reported for graphene–water systems.[20] ABC I, ABC II, and AAB/ABB ices do not have erratic hydrogen bonds and exhibit in-plane order for each layer.

In ABC I trilayer ice, each layer is staggered with respect to the adjacent layer such that the first and third layers are also staggered. Figure S6 shows how each layer in the ABC I ice is staggered with respect to the others.

In the case of ABC II trilayer ice, the staggered hexagon structure characteristic of bilayer ice (Figure 4b) is observed in consecutive layers. For slit widths varying from 10 to 10.4 Å, we observe the formation of ABC II trilayer ice, whose structure is depicted in top-view (Figure 8a) and side-view (Figure 8b) snapshots. Figure 9a–c shows overhead views of two of the three layers, revealing the characteristic stacking arrangements of ABC II trilayer ice. Figure 9d–9f depicts lateral views of the layers of the ABC II ice, with one of the three layers hidden in each case. This trilayer ice is peculiar, in that consecutive layers, such as layers 1 and 2, and 2 and 3, show staggered hexagon structures (Figure 9a,9b). However, layers 1 and 3 exhibit true AB stacking, as depicted in Figure 9c. Every layer of the trilayer ice has an identical triangular arrangement, shown by the comparison of the $g_{OO}(r)$ of each layer, as shown in Figure S7.

AAB or ABB trilayer ices are formed for 11 Å $\geq h \geq 10.6$ Å. Figure 10 depicts the relative alignment of layers for AAB trilayer ice. AAB and ABB ices have different orientations of the same phase: a 180° rotation about the x-axis of the AAB structure (in the XY-plane) yields the ABB structure. Figure S8 shows how this rotation, applied to AAB ice, yields the ABB structure. The convention employed here to distinguish between the two orientations is to view the stacking arrangement from the $+Z$
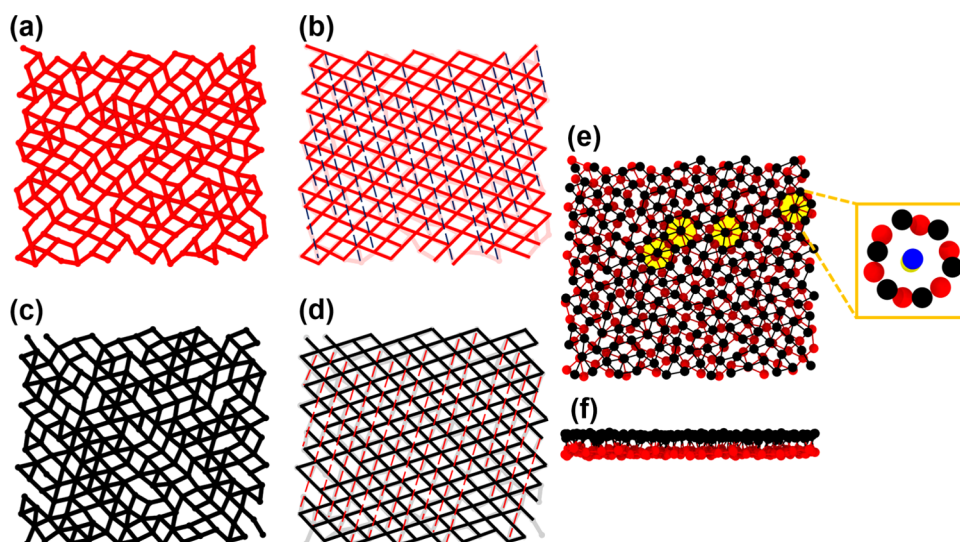
Figure 5. Views of the HBN of a representative system of AB II bilayer ice at 4 GPa and 300 K. The views show only oxygen atoms for clarity. Hydrogen-bonded molecules have been shown to be connected by bonds. Particles are colored in red or black according to their presence in the upper or layer layers. (a) Top view of a portion of the lower layer of the bilayer ice formed. The particles and bonds are red. (b) The HBN of the lower layer has been made translucent, with fictitious lines (full and dotted) laid over it to depict the relative alignment in the ice phase. (c) Top view of the HBN of the upper layer, with bonds and particles colored in black. (d) Fictitious lines have been overlaid upon the translucent HBN of the upper layer, depicting the alignment. (e) Section of the HBN of the entire bilayer. The particles in the upper and lower layers are in black and red, respectively. Hydrogen bonds have been colored halfway according to the particle color. A few representative staggered hexagon structures are highlighted in yellow. The inset shows a close-up view of the staggered hexagon structure, with the central atoms in the upper and lower layers colored in blue and yellow, respectively. (f) Side view of the bilayer ice, depicting the upper and lower layers.
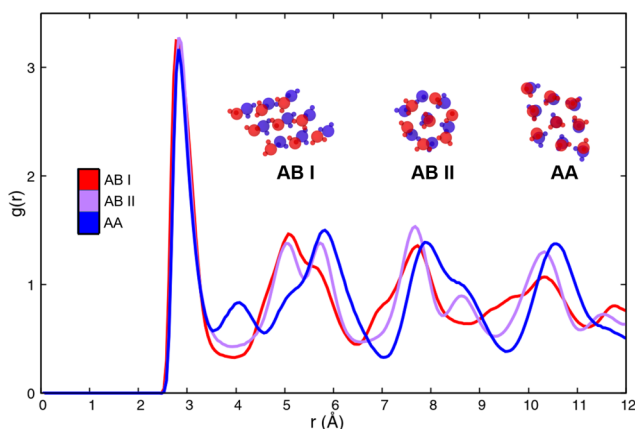

Figure 6. Comparison of the oxygen−oxygen radial distribution functions for AB I, AB II, and AA bilayer ices at 300 K. The insets show characteristic structures of the bilayer ices, with the upper- and lower-layer atoms colored in red and blue, respectively.

Figure 7. Comparison of interlayer hydrogen-bond angle distributions for AB I, AB II, and AA bilayer ices at 300 K. The inset images show the interlayer hydrogen bonds in the YZ-plane.

direction. Since the confining diamond surfaces are identical, the formation of AAB and ABB trilayer ice is equally likely. We have observed that pockets of AAB and ABB ice coexist at the compression-limit pressures. Grain boundaries separate regions of AAB and ABB, whose relative proportions are variable. Figure S9 shows one such grain boundary at 2.1 GPa. In most of the independent simulations carried out, near the compression-limit pressure, we have observed that the ice consists of a few large grains.

Interestingly, as the pressure is increased, the grain boundaries migrate, until one of either orientations, AAB or ABB ice, remains. At high enough lateral pressure, a single grain of either AAB or ABB is observed. Figure 11 shows stages of this grain boundary migration for a particular trajectory, as the pressure is steadily increased. Snapshots are shown for lateral pressures of
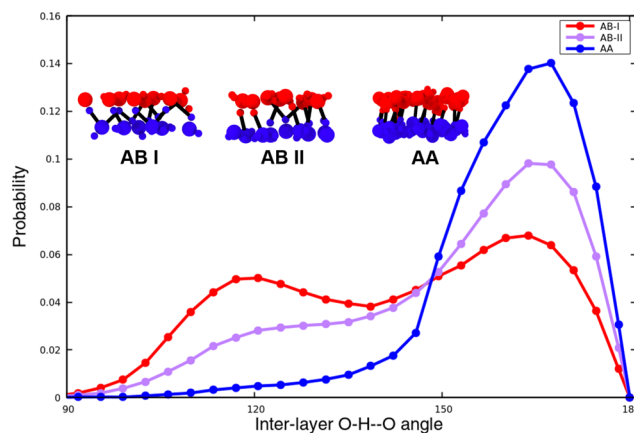
1.8, 2.0, and 2.1 GPa in Figure 11a−c, respectively. By 2.2 GPa, the entire ice is composed of AAB ice of a single orientation, with no trace of ABB ice. We note that the potential energy per molecule and the number of molecules inside the nanochannel remain relatively constant in this pressure range.

Figure S10 depicts the in-plane radial distribution functions of the amorphous trilayer ices ABC I, ABC II, and AAB. ABC II ice, which shows the staggered hexagon motif between adjacent layers, has a $g_{OO}(r)$ that echoes features of both ABC I and AAB ice.

Phase Diagram. Figure 12 shows the compression-limit phase diagram of monolayer, bilayer, and trilayer water. At compression-limit lateral pressures, monolayer, bilayer, and trilayer ices are observed in the ranges $h \in [6, 7.4]$ Å, $h \in [7.5, 8.8]$ Å, and $h \in [9, 11.1]$ Å, respectively. For $h \geq 11.2$ Å, the liquid state is transformed to a four-layered ordered structure,
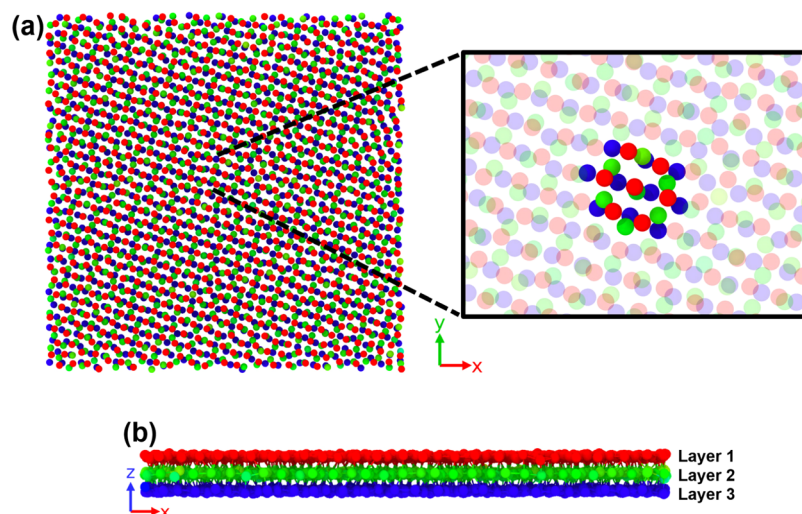
Figure 8. (a) Top view of the *XY*-plane of ABC II trilayer ice, formed at 4 GPa and 300 K, with *h* = 10 Å. The inset shows a close-up view, depicting a stacking order, which is neither ABA nor AAA stacking. (b) Side view of the *XZ*-plane. Only oxygen atoms have been shown for clarity, colored according to their position in each layer.
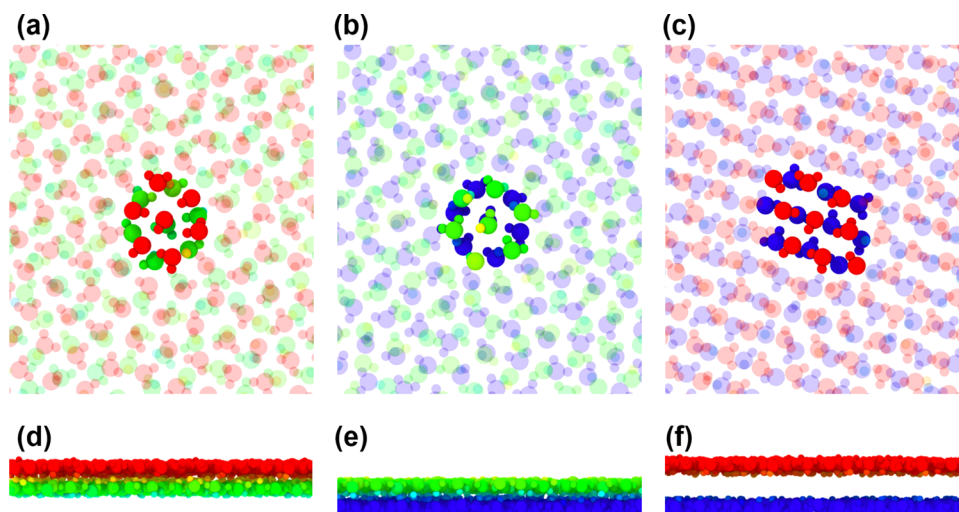

Figure 9. Views of characteristic structures observed in ABC II trilayer ice at 4 GPa and 300 K. Oxygen and hydrogen atoms are colored according to their positions in each layer. (a−c) Top views of a section of the trilayer ice. (d−f) Side views of the layers, showing two out of the three layers in each case.

with two puckered middle layers. The four-layered ice has a stacking scheme that may be described as ABCD.

The compression-limit curves are concave upward, which is also true of analogous quasi-two-dimensional water constrained by graphene.[25] The Clapeyron equation for the two-phase boundaries, which are the compression-limit curves in this case, in a quasi-two-dimensional system is given by[41]

$$\left(\frac{\partial P_{xx}}{\partial h}\right)_T = \frac{f^\alpha - f^\beta}{v^\alpha - v^\beta}$$

where $f = a\Delta P$ is the average force on the confining wall, $\Delta P = P_{zz} - P_{xx}$, a is the water−diamond interfacial area per molecule, v is the volume per molecule, α and β represent the liquid and solid phases, respectively. The existence of the local minima of the compression-limit curves is explained by trends in the equation above. At the optimum value of h, $f^\alpha = f^\beta$, implying that the force exerted on the constraining wall is unaffected by the freezing or melting of the confined water.

The ice−ice phase boundaries (the solid lines denoting the phase boundaries: fMSI−pMSI, pMSI-AB I, AA-ABC I in Figure 12) are steeper, compared to the liquid−ice phase boundaries, and have negative slopes. P_{zz} is the normal component of the pressure tensor, acting on the confining walls. We assume that for a solid−solid boundary, α denotes the lower-density ice and β denotes the higher-density ice. The numerator of the right-hand side of the Clapeyron equation, $f^\alpha - f^\beta$, is large and negative. This is because, when a lower-density ice changes to a higher-density ice, P_{zz} increases faster than P_{xx}, due to an effective increase in the number of water molecules in the high-density phase β. On the other hand, $v^\alpha - v^\beta$ is small and positive since the volume per molecule in the lower-density ice is larger than the volume per molecule occupied by the higher-density ice. These $v^\alpha - v^\beta$ values are smaller than the $v^{liq} - v^{sol}$ values at the liquid−ice phase boundaries (where v^{liq} and v^{sol} refer to the volume per molecule in the liquid and solid phases, respectively), since the water molecules in the liquid state occupy more space than water molecules in the solid phase.
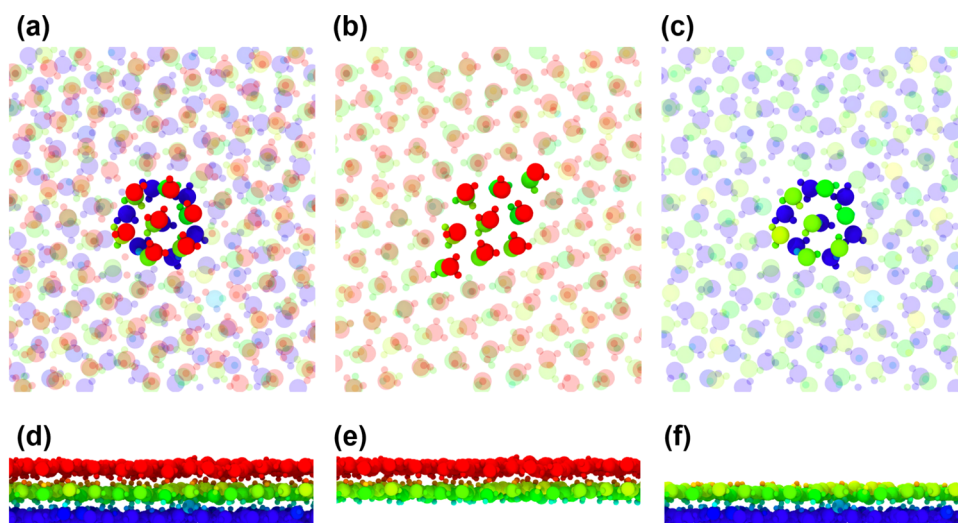
Figure 10. Overhead *XY*-plane views of characteristic structures observed in trilayer AAB ice at 2.9 GPa and 300 K, for a slit width *h* = 10.6 Å. Both oxygen and hydrogen atoms are shown. (a) Top view of all three layers of the AAB trilayer ice. The first two layers show AA stacking. (b, c) *XY*-plane views of a section of the AAB trilayer ice. (d) *XZ*-plane side view of all three layers. (e, f) Side views of sections of (b, c), respectively, showing two out of the three layers in each case.
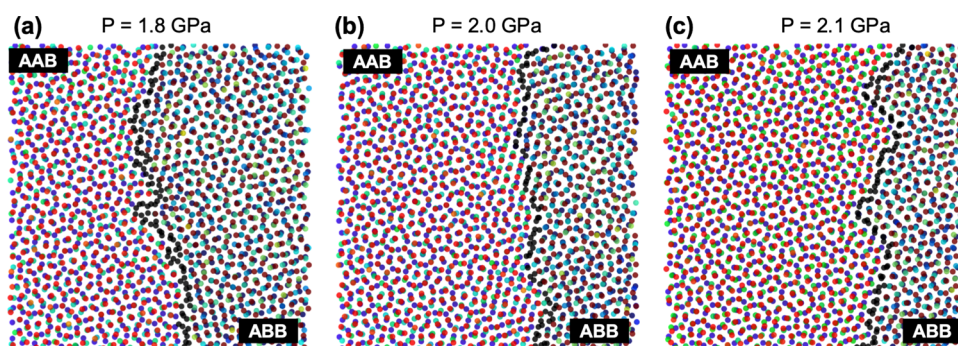

Figure 11. *XY*-plane top views of trilayer ice at (a) 1.8 GPa, (b) 2.0 GPa, and (c) 2.1 GPa at 300 K, for a gap width of 10.6 Å. Only oxygen atoms are shown, colored in blue, green, and red according to their positions in the first, second, and third layers, respectively. AAB and ABB trilayer ices are labeled, with the atoms at the grain boundary colored in black.
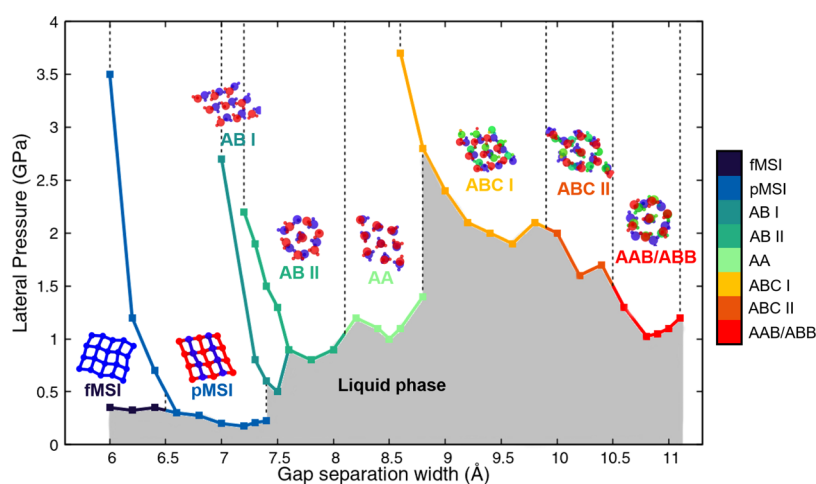

Figure 12. Phase diagram of confined water in the h-P_{xx} plane at a constant temperature (300 K). The filled square symbols denote the lowest lateral pressure at which an ice phase first forms for a particular slit width h. The solid lines connecting the filled symbols, color-coded according to the ice phase, are the compression-limit curves. The dashed black lines separate different phases. The insets depict overhead views of labeled ice structures. Solid-to-solid phase transitions are observed, discernible by the vertical black dotted lines connecting compression-limit curves.

We infer that the sequential formation of the bilayer ices AB I, AB II, and AA with increasing h or P_{xx} may be governed by two competing and opposing influences: the steric effect of water molecules directly over each other in a channel of fixed h, and the

increased strength of such inerratic linear hydrogen bonds. At high enough slit widths ($h > 8.8$ Å) or lateral pressures ($P_{xx} > 2.5$ GPa for $h > 8.5$Å), sufficient water molecules are forced within the nanochannel to create a trilayer phase. We observe a similar competitive trade-off for the trilayer ice phases, between steric effects of the confining geometry and the increased strength of the interlayer inerratic linear hydrogen bonds between layers.

CONCLUSIONS

Molecular simulations have been carried out to study the structural changes of pressure (P_{xx}) and slit width (h) for quasi-two-dimensional water confined in diamond. From simulations performed at lateral pressures of up to 4 GPa, at an ambient temperature of 300 K, we have determined the existence of novel phases AB-II, ABC-I, ABC-II, and AAB/ABB in addition to the previously reported phases AB-I, AA, fMSI, and pMSI. These phases are different from those observed within graphene constrainment. All of the new bilayer and trilayer phases, except ABC I, exhibit a characteristic staggered hexagon substructure.

We explore the $h − P_{xx}$ plane and note its relative insensitivity to the force-field parameters. Even water molecules constrained by highly hydrophilic nanocapillaries form the same ice phases, albeit at different P_{xx}. We have observed that the diamond-constrained fMSI and pMSI formed are structurally similar to those observed within model graphene−water confinement systems. The liquid-to-solid phase transitions for the monolayer ice phases are first-order phase transitions. Within $P_{xx} = 4$ GPa, we have observed fMSI to pMSI solid-to-solid phase transitions, which have not been observed in analogous graphene−water systems in this pressure range. During the solid−solid phase transition from fMSI to pMSI, we qualitatively track the fracturing of the HBN due to point defects and coverage area losses due to puckering.

Of the new bilayer phases, the staggered hexagon phase, AB-II, has characteristics which are intermediate between those of previously discovered phases, AB-I and AA bilayer ices. This difference has been quantified by the relative strength of the interlayer hydrogen-bond stratification. The O−H···O interlayer angle probability distribution of AB-II shows a shoulder peak.

We observe a pressure-driven grain boundary migration between grains of AAB/ABB ice. From a structural point of view, the ABB and AAB phases are identical. AAB and ABB ice have been shown to have orientations of the same trilayer ice phase. Swathes of AAB and ABB ices are present in initially mixed amounts at the compression-limit pressure, separated by grain boundaries. Interestingly, as the lateral pressure is increased, the grain boundaries migrate until one phase dominates completely. The potential energy per molecule for the two phases is also constant, and the average potential energy per molecule remains approximately constant during the grain boundary migration. The dominance of either ABB or AAB is stochastic, with both phases being equally likely during independent simulations of the pressurization process.

The compression-limit curves constructed at a constant temperature, and varying with h, are concave upward in nature. They exhibit points of local minima, corresponding to the optimum h, at which the average force exerted by the ice is unaffected by the freezing transition. For the bilayer and trilayer ice phases, we observe a competitive trade-off between the opposing tendencies of linear interlayer hydrogen-bond strength and the associated cost of the steric effect of water molecules arranged directly over each other.

Diamond has a face-centered cubic Bravais lattice,[42] while graphene has a hexagonal lattice.[43] Even when other influencing factors like hydrophobicity are kept the same, we observe that the qualitative nature of the compression-limit phase diagram for water constrained within model diamond surfaces differs significantly from that of water confined within graphene. Our study further reinforces the importance of the effect of confining geometry on the local environment of water. From our results, we surmise that the lattice structure can strongly influence the templating effect of surfaces. We have explored the complex interplay of interlayer hydrogen bonding, steric effects of water in confinement, and the insensitivity of structures formed by force-field parameters. We envisage that our study will further the understanding of the rich phase behavior of confined water.

ASSOCIATED CONTENT

ⓢ Supporting Information

The Supporting Information is available free of charge at https://pubs.acs.org/doi/10.1021/acs.jpcc.9b11531.

> Schematic of H−O−H and O−H···O angles in fMSI; comparison of fMSI and pMSI using the in-plane radial distribution function and density profiles; transition of fMSI to pMSI taking place in the range of 1−4.8 GPa for a slit width of 6 Å; comparison of projected areas of triangular and tetragonal rings observed in monolayer ice structures; comparison of the oxygen−oxygen radial distribution functions of the upper and lower layers of bilayer ice AB II; views of ABC I trilayer ice; comparison of the oxygen−oxygen radial distribution functions of the three layers of trilayer ice ABC II; depiction of how a 180° rotation about the x-axis, applied to AAB ice yields the ABB ice structure; close-up views of a grain boundary between AAB ice and ABB ice; comparison of the oxygen−oxygen radial distribution functions for ABC I, ABC II, and AAB trilayer ices at 300 K (PDF)

> Abrupt formation of the ordered phase from the liquid state (Movie S1) (AVI)

AUTHOR INFORMATION

Corresponding Author
    Jayant K. Singh − *Department of Chemical Engineering, Indian Institute of Technology Kanpur, Kanpur 208016, India;* ⓘ orcid.org/0000-0001-8056-2115; Phone: 0512-259 6141; Email: jayantks@iitk.ac.in; Fax: 0512-259 0104

Author
    Amrita Goswami − *Department of Chemical Engineering, Indian Institute of Technology Kanpur, Kanpur 208016, India;* ⓘ orcid.org/0000-0001-8706-2383

Complete contact information is available at:
https://pubs.acs.org/10.1021/acs.jpcc.9b11531

Notes
The authors declare no competing financial interest.

ACKNOWLEDGMENTS

and help in preparing the initial systems. He also thanks R. Goswami for his invaluable support and insightful discussions.

■ REFERENCES

(1) Salzmann, C. G.; Radaelli, P. G.; Slater, B.; Finney, J. L. The Polymorphism of Ice: Five Unresolved Questions. *Phys. Chem. Chem. Phys.* **2011**, *13*, 18468.

(2) Kamb, B. Ice Under Stress and Pressure, Ice in Order and Disorder. *Eng. Sci.* **1967**, *31*, 27−33.

(3) Kamb, B.; Davis, B. L. Ice VII, the Densest Form of Ice. *Proc. Natl. Acad. Sci. U.S.A.* **1964**, *52*, 1433−1439.

(4) Bina, C. R.; Navrotsky, A. Possible Presence of High-Pressure Ice in Cold Subducting Slabs. *Nature* **2000**, *408*, 844−847.

(5) Tschauner, O.; Huang, S.; Greenberg, E.; Prakapenka, V. B.; Ma, C.; Rossman, G. R.; Shen, A. H.; Zhang, D.; Newville, M.; Lanzirotti, A.; et al. Ice-VII Inclusions in Diamonds: Evidence for Aqueous Fluid in Earthas Deep Mantle. *Science* **2018**, *359*, 1136−1139.

(6) Kagi, H.; Lu, R.; Davidson, P.; Goncharov, A. F.; Mao, H. K.; Hemley, R. J. Evidence for Ice VI as an Inclusion in Cuboid Diamonds from High P-T near Infrared Spectroscopy. *Mineral. Mag.* **2000**, *64*, 1089−1097.

(7) Dziewonski, A. M.; Anderson, D. L. Preliminary Reference Earth Model. *Phys. Earth Planet. Inter.* **1981**, *25*, 297−356.

(8) Katsura, T.; Yoneda, A.; Yamazaki, D.; Yoshino, T.; Ito, E. Adiabatic Temperature Profile in the Mantle. *Phys. Earth Planet. Inter.* **2010**, *183*, 212−218.

(9) Salzmann, C. G. Advances in the Experimental Exploration of Water's Phase Diagram. *J. Chem. Phys.* **2019**, *150*, No. 060901.

(10) Gelb, L. D.; Gubbins, K. E.; Radhakrishnan, R.; Sliwinska-Bartkowiak, M. Phase Separation in Confined Systems. *Rep. Prog. Phys.* **1999**, *62*, 1573−1659.

(11) Algara-Siller, G.; Lehtinen, O.; Wang, F. C.; Nair, R. R.; Kaiser, U.; Wu, H. A.; Geim, A. K.; Grigorieva, I. V. Square Ice in Graphene Nanocapillaries. *Nature* **2015**, *519*, 443−445.

(12) Agrawal, K. V.; Shimizu, S.; Drahushuk, L. W.; Kilcoyne, D.; Strano, M. S. Observation of Extreme Phase Transition Temperatures of Water Confined inside Isolated Carbon Nanotubes. *Nat. Nanotechnol.* **2017**, *12*, 267−273.

(13) Zhao, W.-H.; Bai, J.; Yuan, L.-F.; Yang, J.; Zeng, X. C. Ferroelectric Hexagonal and Rhombic Monolayer Ice Phases. *Chem. Sci.* **2014**, *5*, 1757−1764.

(14) Takaiwa, D.; Hatano, I.; Koga, K.; Tanaka, H. Phase Diagram of Water in Carbon Nanotubes. *Proc. Natl. Acad. Sci. U.S.A.* **2008**, *105*, 39−43.

(15) Bai, J.; Angell, C. A.; Zeng, X. C. Guest-Free Monolayer Clathrate and its Coexistence with Two-dimensional High-density Ice. *Proc. Natl. Acad. Sci. U.S.A.* **2010**, *107*, 5718−5722.

(16) Chen, J.; Schusteritsch, G.; Pickard, C. J.; Salzmann, C. G.; Michaelides, A. Two Dimensional Ice from First Principles: Structures and Phase Transitions. *Phys. Rev. Lett.* **2016**, *116*, No. 025501.

(17) Koga, K.; Tanaka, H.; Zeng, X. C. First-Order Transition in Confined Water between High-Density Liquid and Low-Density Amorphous Phases. *Nature* **2000**, *408*, 564−567.

(18) Zangi, R.; Mark, A. E. Monolayer Ice. *Phys. Rev. Lett.* **2003**, *91*, No. 025502.

(19) Bai, J.; Zeng, X. C. Polymorphism and Polyamorphism in Bilayer Water Confined to Slit Nanopore under High Pressure. *Proc. Natl. Acad. Sci. U.S.A.* **2012**, *109*, 21240−21245.

(20) Zhu, Y.; Wang, F.; Bai, J.; Zeng, X. C.; Wu, H. Formation of Trilayer Ices in Graphene Nanocapillaries under High Lateral Pressure. *J. Phys. Chem. C* **2016**, *120*, 8109−8115.

(21) Corsetti, F.; Zubeltzu, J.; Artacho, E. Enhanced Configurational Entropy in High-Density Nanoconfined Bilayer Ice. *Phys. Rev. Lett.* **2016**, *116*, No. 085901.

(22) Giovambattista, N.; Rossky, P. J.; Debenedetti, P. G. Phase Transitions Induced by Nanoconfinement in Liquid Water. *Phys. Rev. Lett.* **2009**, *102*, No. 050603.

(23) Han, S.; Choi, M. Y.; Kumar, P.; Stanley, H. E. Phase Transitions in Confined Water Nanofilms. *Nat. Phys.* **2010**, *6*, 685−689.

(24) Kastelowitz, N.; Johnston, J. C.; Molinero, V. The Anomalously High Melting Temperature of Bilayer Ice. *J. Chem. Phys.* **2010**, *132*, No. 124511.

(25) Zhu, Y.; Wang, F.; Bai, J.; Zeng, X. C.; Wu, H. Compression Limit of Two-Dimensional Water Constrained in Graphene Nanocapillaries. *ACS Nano* **2015**, *9*, 12197−12204.

(26) Straumanis, M. E.; Aka, E. Z. Precision Determination of Lattice Parameter, Coefficient of Thermal Expansion and Atomic Weight of Carbon in Diamond. *J. Am. Chem. Soc.* **1951**, *73*, 5643−5646.

(27) Gražulis, S.; Chateigner, D.; Downs, R. T.; Yokochi, A. F. T.; Quirós, M.; Lutterotti, L.; Manakova, E.; Butkus, J.; Moeck, P.; Bail, A. L. Crystallography Open Database − an Open-Access Collection of Crystal Structures. *J. Appl. Crystallogr.* **2009**, *42*, 726−729.

(28) Yang, L.; Guo, Y.; Diao, D. Structure and Dynamics of Water Confined in a Graphene Nanochannel under Gigapascal High Pressure: Dependence of Friction on Pressure and Confinement. *Phys. Chem. Chem. Phys.* **2017**, *19*, 14048−14054.

(29) Plimpton, S. Fast Parallel Algorithms for Short-Range Molecular Dynamics. *J. Comput. Phys.* **1995**, *117*, 1−19.

(30) Abascal, J. L. F.; Vega, C. A General Purpose Model for the Condensed Phases of Water: TIP4P/2005. *J. Chem. Phys.* **2005**, *123*, No. 234505.

(31) Dix, J.; Lue, L.; Carbone, P. Why Different Water Models Predict Different Structures under 2D Confinement. *J. Comput. Chem.* **2018**, *39*, 2051−2059.

(32) Shergold, H.; Hartley, C. The Surface Chemistry of Diamond. *Int. J. Miner. Process.* **1982**, *9*, 219−233.

(33) Werder, T.; Walther, J. H.; Jaffe, R. L.; Halicioglu, T.; Koumoutsakos, P. On the Water-Carbon Interaction for Use in Molecular Dynamics Simulations of Graphite and Carbon Nanotubes. *J. Phys. Chem. B* **2003**, *107*, 1345−1352.

(34) Zhu, Y.; Wang, F.; Wu, H. Superheating of Monolayer Ice in Graphene Nanocapillaries. *J. Chem. Phys.* **2017**, *146*, No. 134703.

(35) Ostrovskaya, L.; Perevertailo, V.; Ralchenko, V.; Dementjev, A.; Loginova, O. Wettability and Surface Energy of Oxidized and Hydrogen Plasma-Treated Diamond Films. *Diamond Relat. Mater.* **2002**, *11*, 845−850.

(36) Tagawa, M.; Ikemura, M.; Nakayama, Y.; Ohmae, N. Effect of Water Adsorption on Microtribological Properties of Hydrogenated Diamond-Like Carbon Films. *Tribol. Lett.* **2004**, *17*, 575−580.

(37) Ostrovskaya, L.; Perevertailo, V.; Ralchenko, V.; Saveliev, A.; Zhuravlev, V. Wettability of Nanocrystalline Diamond Films. *Diamond Relat. Mater.* **2007**, *16*, 2109−2113.

(38) Stukowski, A. Visualization and Analysis of Atomistic Simulation Data with OVITO−the Open Visualization Tool. *Modell. Simul. Mater. Sci. Eng.* **2009**, *18*, No. 015012.

(39) Goswami, A.; Singh, J. K. A General Topological Network Criterion for Exploring the Structure of Icy Nanoribbons and Monolayers. *Phys. Chem. Chem. Phys.* **2020**, DOI: 10.1039/c9cp04902a.

(40) Goswami, R.; Goswami, A.; Singh, J. K. d-SEAMS: Deferred Structural Elucidation Analysis for Molecular Simulations.

(41) Koga, K.; Tanaka, H. Phase Diagram of Water between Hydrophobic Surfaces. *J. Chem. Phys.* **2005**, *122*, No. 104711.

(42) Wyckoff, R. W. G. *Crystal Structures*, 2nd ed.; Interscience Publishers: New York, 1963; Vol. 1.

(43) Howe, J. Y.; Rawn, C. J.; Jones, L. E.; Ow, H. Improved Crystallographic Data for Graphite. *Powder Diffr.* **2003**, *18*, 150−154.